



Cite this: DOI: 10.1039/c9cc10036a

 Received 28th December 2019,  
Accepted 7th February 2020

DOI: 10.1039/c9cc10036a

rsc.li/chemcomm

# Cobalt decorated nitrogen-doped carbon bowls as efficient electrocatalysts for the oxygen reduction reaction†

 Haobin Zhong, Changwei Shi, Jiantao Li, Ruohan Yu, Qiang Yu, Haoyun Liu, Yao Yao, Jinsong Wu,  Liang Zhou \* and Liqiang Mai \*

**Cobalt decorated nitrogen-doped carbon bowls (Co@NCB) have been successfully constructed by impregnating bowl-like resin particles with cobalt salt followed by annealing. The cobalt exists in the following two forms in the obtained Co@NCB: Co nanoparticles and CoN<sub>4</sub>. The Co@NCB outperforms the commercial Pt/C in the oxygen reduction reaction in terms of half-wave potential and stability. When Co@NCB is applied in zinc–air batteries, a high open-circuit voltage, excellent power density, and satisfactory stability are achieved.**

Developing renewable and clean energy technologies is quite necessary on account of the rising energy demand, climate change, and pollution resulting from burning fossil energy.<sup>1–5</sup> Metal–air batteries are expected to be potential substitutes for conventional internal combustion engines to power cars.<sup>6,7</sup> However, the electrochemical oxygen reduction reaction (ORR) is rather slow, restricting the energy conversion efficiency.<sup>8,9</sup> Although noble-metal catalysts have been widely applied owing to their high catalytic performance, they are hindered by high cost and low stability.<sup>10–12</sup> Hence, it is imperative to develop low-cost, durable, and highly efficient nonprecious metal ORR catalysts.

Recently, great advances have been made in enhancing the activity of nonprecious catalysts to a level comparable to that of noble-metal materials.<sup>13–17</sup> The key characteristic of this kind of catalyst is the presence of transition metal–nitrogen species (M–N<sub>x</sub>) anchored on carbon materials.<sup>18–23</sup> Zelenay *et al.* used polyaniline as a carbon/nitrogen precursor to incorporate Fe/Co and obtained PANI–Fe/Co/FeCo–C catalysts with relatively ideal ORR performance.<sup>24</sup> Qiao *et al.* developed a Fe–N–C catalyst consisting of ordered macroporous carbon interlinked with carbon nanotubes.<sup>25</sup> Yang *et al.* reported a Co–N–C catalyst with desirable ORR activity.<sup>26</sup> Although progress has been made extensively, it is still an extremely important research area to design highly active ORR catalysts, which can surpass the performance of noble-metal materials.

State Key Laboratory of Advanced Technology for Materials Synthesis and Processing, Wuhan University of Technology, Wuhan 430070, P. R. China.  
E-mail: liangzhou@whut.edu.cn, mlq518@whut.edu.cn

† Electronic supplementary information (ESI) available. See DOI: 10.1039/c9cc10036a

Besides chemical composition, the structure of ORR catalysts also plays a key role in the electrocatalytic performance. A stable porous carbon supporting structure can not only increase the specific surface area but also improve the electric conductivity. Mai *et al.* reported atomic Co dispersed on nitrogen-doped graphene, exhibiting excellent ORR performance.<sup>27</sup> Cho *et al.* employed commercially available melamine foam as a unique architecture for the ORR.<sup>28</sup> Feng *et al.* designed a Fe/N doped hollow carbon catalyst, which demonstrated efficient ORR performance under acidic/alkaline conditions.<sup>29</sup>

Carbon spheres have been extensively studied as supporting materials for electrocatalysis, owing to their easy preparation and large surface area.<sup>30–32</sup> However, the contact area between different carbon spheres is relatively small, which is disadvantageous for electron transport. This would limit the overall performance of carbon spheres for the ORR. A hollow bowl-like structure is an ideal morphology to address the aforementioned issue. Compared with carbon spheres, hollow carbon bowls stacked with each other are beneficial to conductivity.<sup>33</sup> When compared to conventional hollow spheres, the hollow bowl-like structure reduces the void space and more bowls can be packed tightly in a certain volume, enabling more active sites presented in the same volume.<sup>34</sup>

Herein, we present a facile route to construct cobalt decorated nitrogen-doped carbon bowls (Co@NCB) as high-efficiency ORR catalysts. The primary synthetic strategy is illustrated in Fig. 1. First, monodisperse SiO<sub>2</sub>@resorcinol-formaldehyde (SiO<sub>2</sub>@RF, Fig. S1, ESI†) microspheres were prepared *via* a well-known sol-gel process.<sup>35–37</sup> RF hollow bowls (RFB, Fig. S2, ESI†) were obtained by etching the SiO<sub>2</sub>@RF with HF. Then, the RF hollow bowls were mixed with cobalt acetate to obtain Co<sup>2+</sup>@RF bowls through an impregnation method. Finally, with subsequent pyrolysis at 800 °C under NH<sub>3</sub> flow, the Co@NCB was achieved. For comparison, carbon bowls (CB, Fig. S3, ESI†), nitrogen-doped carbon bowls (NCB, Fig. S4, ESI†), Co@NCB with acid treatment (Co@NCB-AT, Fig. S5, ESI†) and cobalt decorated carbon bowls (Co@CB, Fig. S6a and b, ESI†) were prepared as control samples.

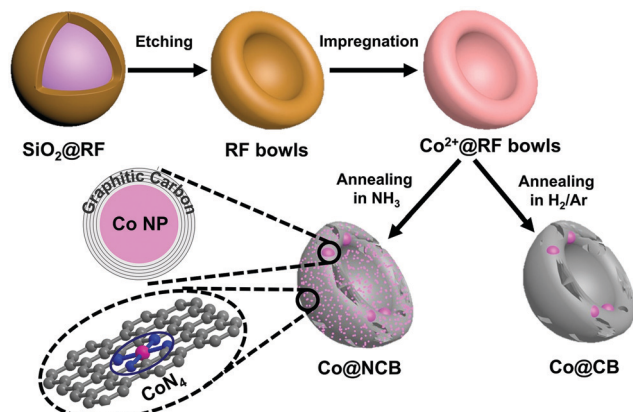


Fig. 1 Schematic illustration for the synthesis of Co@NCB.

The microstructure of Co@NCB is characterized by scanning electron microscopy (SEM) and transmission electron microscopy (TEM). The Co@NCB presents a well-defined bowl-like morphology. The diameter and the central cavity size of Co@NCB are  $\sim 300$  and  $150$  nm, respectively (Fig. 2a). Compared to the smooth surface of RFB (Fig. S2, ESI<sup>†</sup>), CB (Fig. S3, ESI<sup>†</sup>), and NCB (Fig. S4, ESI<sup>†</sup>), the Co@NCB displays a much rougher surface with unevenly distributed irregular cracks. These irregular cracks may cause a larger specific surface area and are beneficial to the exposure of active sites. Similar cracks can be observed on the surface of Co@CB, suggesting that the existence of Co species induces the formation of such cracks during the high-temperature annealing. The TEM image (Fig. 2b) shows the existence of Co nanoparticles (Co NPs indicated by red circles) with a diameter of  $\sim 30$ – $50$  nm in Co@NCB. A high-resolution TEM image demonstrates that Co NPs are highly crystalline with clear lattice fringes and the Co NPs are well-encapsulated in highly graphitic carbon layers with an interplanar distance of  $0.34$  nm (Fig. 2c). Energy dispersive X-ray (EDX) mapping analysis demonstrates that the Co not only concentrates on black NPs but also evenly distributes in

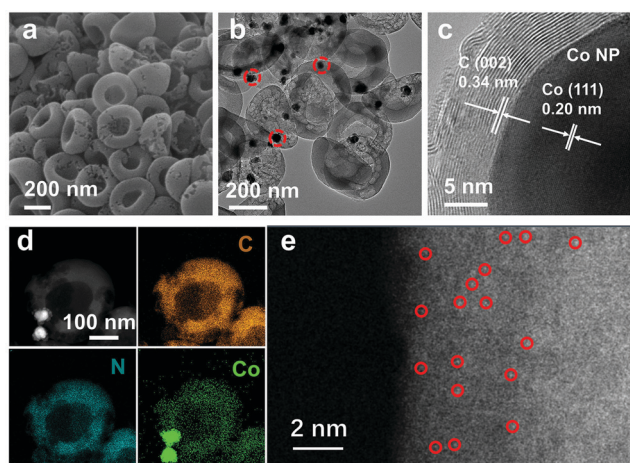


Fig. 2 (a) SEM image of Co@NCB, (b) TEM image of Co@NCB, (c) high-resolution TEM image of Co@NCB, and (d) EDX mappings of Co@NCB. (e) Aberration-corrected STEM image of Co@NCB-AT.

other regions of the hollow bowls (Fig. 2d). At regions beyond the Co NPs, the Co exists most likely in the form of  $\text{CoN}_4$ . To prove this speculation, aberration-corrected scanning transmission electron microscopy (STEM) is applied to Co@NCB-AT, and single Co atoms (indicated by red circles in Fig. 2e) can be clearly observed. The aberration-corrected STEM is not applied to Co@NCB due to the magnetic feature of Co NPs. As for Co@CB (Fig. S6, ESI<sup>†</sup>), Co NPs can also be clearly observed. However, at regions beyond Co NPs, the signal for Co is much weaker than that of Co@NCB, demonstrating that the annealing in  $\text{NH}_3$  induces the formation of atomically dispersed  $\text{CoN}_4$  (Fig. S6d–f, ESI<sup>†</sup>).

The X-ray diffraction (XRD; Fig. S7a, ESI<sup>†</sup>) patterns of Co@NCB and Co@CB show the (002) diffraction peak for the graphitic carbon at  $26.3^\circ$  and the (111), (200), and (220) diffractions for the face-centered cubic Co (PDF # 015-0806) at  $44.2^\circ$ ,  $51.5^\circ$  and  $75.9^\circ$ , respectively. However, the Co@NCB displays a graphitic carbon diffraction peak much stronger than that of Co@CB. Both Co@NCB and Co@CB show typical D and G bands in the Raman spectra (Fig. S7b, ESI<sup>†</sup>). The  $I_D/I_G$  ratio of Co@NCB is  $0.99$ , which is much lower than that of Co@CB ( $1.57$ ). Both the XRD and Raman results demonstrate that the graphitization degree of Co@NCB is much higher than that of Co@CB, implying that the introduction of N-doping in carbon may lower the graphitization temperature.

X-ray photoelectron spectroscopy (XPS) reveals the elemental compositions of the catalysts. The XPS survey spectrum (Fig. 3a) suggests that the Co@NCB consists of C, N, O, and Co. Four types of nitrogen species can be identified from the N 1s spectrum (Fig. 3b) as follows: pyridinic-N ( $\sim 398.2$  eV),  $\text{CoN}_4$  ( $\sim 399.1$  eV), graphitic-N ( $\sim 400.7$  eV), and oxidized-N ( $\sim 402.5$  eV).<sup>38,39</sup> The Co 2p<sub>3/2</sub> spectrum (Fig. 3c) presents four components, which can be ascribed to the  $\text{CoN}_4$  moieties ( $781.7$  eV),  $\text{Co}_x\text{O}_y$  ( $\sim 780.3$  eV), and satellites ( $783.8$  and  $786.3$  eV).<sup>40</sup> As for Co@CB, no N signal can be detected from the XPS survey spectrum (Fig. S8a, ESI<sup>†</sup>). In addition, the component for  $\text{CoN}_4$  is absent in the Co 2p<sub>3/2</sub> spectrum (Fig. S8b, ESI<sup>†</sup>). It should be noted that neither Co@NCB nor Co@CB displays the component for metallic Co,

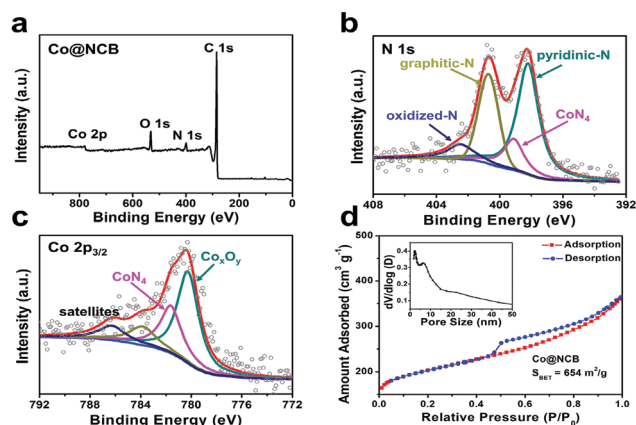


Fig. 3 (a) XPS survey spectrum, (b) high-resolution N 1s XPS spectrum, (c) high-resolution Co 2p XPS spectrum, and (d) nitrogen adsorption-desorption isotherm and the corresponding BJH pore size distribution of Co@NCB.

which may be caused by the encapsulation of metallic Co in the carbon shells and surface oxidation of Co NPs.

To further explore the surface area and porosity, the  $N_2$  adsorption/desorption isotherms are shown in Fig. 3d. Both mesopores and micropores co-exist in Co@NCB, giving rise to a surface area of  $654 \text{ m}^2 \text{ g}^{-1}$ . Such a high surface area is advantageous to the exposure of active centers for the ORR. In general, the mesopores are in favour of the mass transfer and the micropores would offer more active sites.<sup>19</sup> The Co@CB ( $576 \text{ m}^2 \text{ g}^{-1}$ ) and Co@NCB-AT ( $610 \text{ m}^2 \text{ g}^{-1}$ ) show a surface area slightly lower than that of Co@NCB (Fig. S9, ESI<sup>†</sup>). The Co contents are determined by thermogravimetric analysis (Fig. S10, ESI<sup>†</sup>). The Co@NCB, Co@CB, and Co@NCB-AT have Co contents (including both metallic and single-atom Co) of 12.4, 7.8, and 5.2 wt%, respectively.

The ORR performances of Co@NCB, CB, NCB, Co@NCB-AT, Co@CB, and commercial Pt/C (20 wt%) are evaluated by cyclic voltammetry (CV, Fig. 4a) first. The Co@NCB shows an obvious oxygen reduction peak at 0.84 V. This peak is more positive than those of CB (0.67 V), Co@CB (0.76 V), NCB (0.77 V), and Co@NCB-AT (0.81 V), and it is also closest to the peak of Pt/C (0.87 V). Besides, the Co@NCB displays a half-wave potential of 0.851 V, which is higher than those of Pt/C (0.845 V), CB (0.679 V), Co@CB (0.735 V), NCB (0.731 V), and Co@NCB-AT (0.793 V) (Fig. 4b). To reveal the origin of the ORR activity,  $\text{SCN}^-$  is employed to block the  $\text{CoN}_4$  active sites of Co@NCB. The ORR activity decreases significantly with the introduction of  $\text{SCN}^-$ , demonstrating the active role of  $\text{CoN}_4$  in catalyzing the ORR (Fig. S11, ESI<sup>†</sup>).<sup>26</sup> In contrast, the metallic Co NPs also play a significant role in the ORR. By etching the Co NPs away from Co@NCB using  $\text{H}_2\text{SO}_4$ , the obtained Co@NCB-AT displays an ORR performance much inferior to that of Co@NCB.

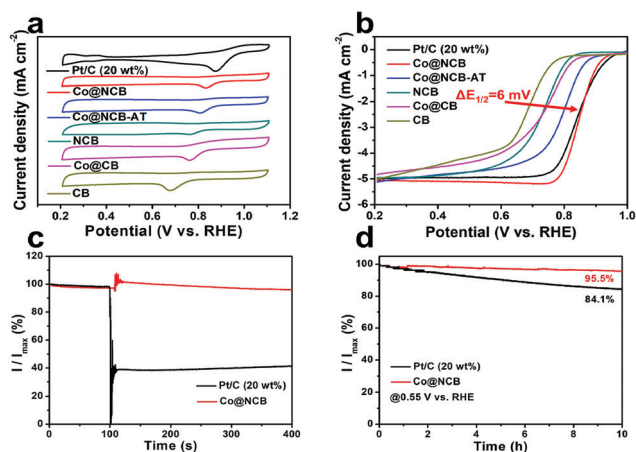


Fig. 4 ORR performances of Co@NCB, CB, NCB, Co@NCB-AT, Co@CB, and Pt/C (20 wt%) in 0.1 M KOH solution saturated with  $\text{O}_2$  at room temperature. (a) CV curves at a scan rate of  $5 \text{ mV s}^{-1}$ . (b) Linear sweep voltammetry (LSV) curves at  $5 \text{ mV s}^{-1}$  and 1600 rpm. (c) Chronoamperometric responses of Co@NCB and Pt/C at a potential of 0.55 V in  $\text{O}_2$ -saturated 0.1 M KOH solution (150 mL) at a rotation speed of 1600 rpm with the addition of methanol (9 mL) at 100 s. (d) Current-time chronoamperometric responses of Co@NCB and Pt/C in  $\text{O}_2$ -saturated 0.1 M KOH at 0.55 V and 1600 rpm.

The aforementioned results indicate that the co-existence of  $\text{CoN}_4$  and Co NPs is vital for achieving high ORR activity. It is postulated that the Co NPs may boost the ORR activity of  $\text{CoN}_4$  by changing its electronic structure.

The methanol tolerances of Co@NCB and Pt/C are compared in Fig. 4c. When 9 mL methanol is introduced, there is an instant decline in current for Pt/C. In contrast, the current of Co@NCB remains almost unchanged after shaking a bit, demonstrating its excellent methanol tolerance. The stabilities of Co@NCB and Pt/C are also examined *via* chronoamperometric responses (Fig. 4d). After a stability test of 10 h, 95.5% of the original current density is remained for Co@NCB, which is better than that of Pt/C (84.1%).

The ORR performances under acidic conditions are also tested. The half-wave potential of Co@NCB is not comparable to that of Pt/C in  $\text{HClO}_4$  solution (Fig. S12a, ESI<sup>†</sup>). However, the stability of Co@NCB is better than that of Pt/C (Fig. S12b, ESI<sup>†</sup>).

Rotating disk electrode (RDE) measurements are used to study the reaction mechanism and the electron transfer pathway (Fig. S12c, ESI<sup>†</sup>). The Koutecky–Levich (K–L) plots show a good linearity and parallelism in the potential range of 0.3–0.7 V (Fig. S12d, ESI<sup>†</sup>). The electron-transfer number ( $n$ ) of Co@NCB is determined to be  $\sim 3.9$ , suggesting the 4-electron ( $4e$ ) ORR process and  $\text{O}_2$  is basically reduced to  $\text{OH}^-$ . The rotating ring disk electrode (RRDE) test shows an  $n$  value close to 4 (Fig. S13, ESI<sup>†</sup>). Meanwhile, the  $\text{H}_2\text{O}_2$  yield is relatively low ( $\approx 5\%$ ). The Co@NCB is benchmarked with Pt/C toward the ORR. All above results show that the Co@NCB displays better electrocatalytic performance than the Pt/C and other control samples in general. Moreover, the performance is superior to those of many previously reported Co-based catalysts (Table S1, ESI<sup>†</sup>).

To further explore the application of Co@NCB, the electrochemical performance in primary zinc–air batteries is tested. The open circuit voltage of the battery based on Co@NCB exceeds 1.4 V, which is similar to that of the battery based on Pt/C (Fig. 5a). The voltage of the Co@NCB-based battery surpasses that of the Pt/C-based battery in the high current density zone ( $> 75 \text{ mA cm}^{-2}$ ). In addition, the power density reaches  $275 \text{ mW cm}^{-2}$ , which is higher than that of the Pt/C-based battery ( $262 \text{ mW cm}^{-2}$ ). Galvanostatic discharge tests at different current densities are performed to explore the stability of the material. After the 10 h test at  $10 \text{ mA cm}^{-2}$ , there is almost no voltage decay for both Co@NCB- and Pt/C-based batteries (Fig. 5b). However, after the 10 h test at  $200 \text{ mA cm}^{-2}$ , there is a significant voltage drop for the Pt/C-based battery, while the

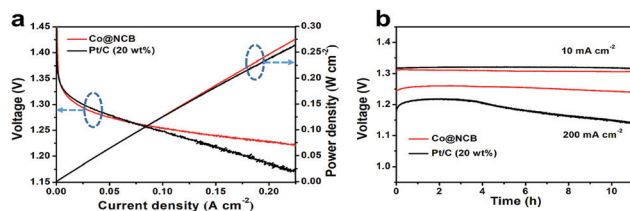


Fig. 5 Electrochemical performances of Co@NCB and Pt/C (20 wt%) in primary zinc–air batteries. (a) Discharge polarization curves and corresponding power density of Co@NCB and Pt/C. (b) Galvanostatic discharge curves of Co@NCB and Pt/C tested at 10 and  $200 \text{ mA cm}^{-2}$ .

Co@NCB-based battery demonstrates a very stable discharge voltage.

In conclusion, Co-decorated N-doped carbon bowls (Co@NCB) are synthesized *via* a facile method. The obtained Co@NCB manifests a desirable ORR activity and durability, surpassing the Pt/C. The Co@NCB also demonstrates remarkable performance in primary zinc-air batteries. The co-existence of CoN<sub>4</sub> and Co NPs in Co@NCB is vital to the improved ORR performance.

This work was supported by the National Natural Science Foundation of China (21673171), and the Yellow Crane Talent (Science & Technology) Program of Wuhan City.

## Conflicts of interest

There are no conflicts to declare.

## Notes and references

- M. Shao, Q. Chang, J. P. Dodelet and R. Chenitz, *Chem. Rev.*, 2016, **116**, 3594–3657.
- P. Simon, Y. Gogotsi and B. Dunn, *Science*, 2014, **343**, 1210.
- B. Y. Guan, L. Yu and X. W. Lou, *J. Am. Chem. Soc.*, 2016, **138**, 11306.
- Y. Jia, K. Jiang, H. T. Wang and X. D. Yao, *Chem*, 2019, **5**, 1371.
- X. C. Yan, Y. Jia and X. D. Yao, *Chem. Soc. Rev.*, 2018, **47**, 7628–7658.
- J. Zhang, Z. Zhao, Z. Xia and L. Dai, *Nat. Nanotechnol.*, 2015, **10**, 444.
- Y. Li and H. Dai, *Chem. Soc. Rev.*, 2014, **43**, 5257.
- Y. Yuan, L. Yang, B. He, E. Pervaiz, Z. Shao and M. Yang, *Nanoscale*, 2017, **9**, 6259–6263.
- J. S. Li, J. J. Chen, H. Y. Wang, Y. Ren, K. Liu, Y. G. Tang and M. H. Shao, *Energy Storage Mater.*, 2017, **8**, 49–58.
- C. Cui, L. Gan, M. Heggen, S. Rudi and P. Strasser, *Nat. Mater.*, 2013, **12**, 765–771.
- D. Wang, H. L. Xin, R. Hovden, H. Wang, Y. Yu, D. A. Muller, F. J. DiSalvo and H. D. Abruña, *Nat. Mater.*, 2013, **12**, 81–87.
- Y. Jia, L. Z. Zhang, A. J. Du, G. P. Gao, J. Chen, X. C. Yan, C. L. Brown and X. D. Yao, *Adv. Mater.*, 2016, **28**, 9532–9538.
- F. Jaouen, E. Proietti, M. Lefèvre, R. Chenitz, J.-P. Dodelet, G. Wu, H. T. Chung, C. M. Johnston and P. Zelenay, *Energy Environ. Sci.*, 2011, **4**, 114–130.
- K. Strickland, E. Miner, Q. Jia, U. Tylus, N. Ramaswamy, W. Liang, M.-T. Sougrati, F. Jaouen and S. Mukerjee, *Nat. Commun.*, 2015, **6**, 7343.
- X. Y. Li, Q. Q. Jiang, S. Dou, L. B. Deng, J. Huo and S. Y. Wang, *J. Mater. Chem. A*, 2016, **4**, 15836.
- X. X. Yan, K. X. Liu, T. Wang, Y. You, J. G. Liu, P. Wang, X. Q. Pan, G. F. Wang, J. Luo and J. Zhu, *J. Mater. Chem. A*, 2017, **5**, 3336.
- B. You, N. Jiang, M. L. Sheng, W. S. Drisdell, J. Yano and Y. J. Sun, *ACS Catal.*, 2015, **5**, 7068.
- B. Y. Guan, L. Yu and X. W. Lou, *Adv. Sci.*, 2017, **4**, 1700247.
- T. T. Feng and M. N. Zhang, *Chem. Commun.*, 2018, **54**, 11570–11573.
- J. Sun, Y. H. Fang and Z. P. Liu, *Phys. Chem. Chem. Phys.*, 2014, **16**, 13733–13740.
- S. Kattel, P. Atanassov and B. Kiefer, *J. Phys. Chem. C*, 2012, **116**, 17378–17383.
- Y. Y. Liu, H. L. Jiang, Y. H. Zhu, X. L. Yang and C. Z. Li, *J. Mater. Chem. A*, 2016, **4**, 1694.
- Y. J. Zhang, L. H. Lu, S. Zhang, Z. Z. Lv, D. T. Yang, J. H. Liu, Y. Chen, X. C. Tian, H. Y. Jin and W. G. Song, *J. Mater. Chem. A*, 2018, **6**, 5740.
- G. Wu, K. L. More, C. M. Johnston and P. Zelenay, *Science*, 2011, **332**, 443–447.
- J. Liang, R. F. Zhou, X. M. Chen, Y. H. Tang and S. Z. Qiao, *Adv. Mater.*, 2014, **26**, 6074–6079.
- Q. Q. Cheng, L. J. Yang, L. L. Zou, Z. Q. Zou, C. Chen, Z. Hu and H. Yang, *ACS Catal.*, 2017, **7**, 6864–6871.
- J. T. Li, H. Y. Liu, M. M. Wang, C. Lin, W. Yang, J. S. Meng, Y. N. Xu, K. A. Owusu, B. L. Jiang, C. X. Chen, D. N. Fan, L. Zhou and L. Q. Mai, *Chem. Commun.*, 2019, **55**, 334–337.
- J. S. Lee, G. S. Park, S. T. Kim, M. L. Liu and J. Cho, *Angew. Chem., Int. Ed.*, 2013, **52**, 1026–1030.
- Y. Wang, A. G. Kong, X. T. Chen, Q. P. Lin and P. Y. Feng, *ACS Catal.*, 2015, **5**, 3887–3893.
- H. Wang, X. J. Bo, A. X. Wang and L. P. Guo, *Electrochem. Commun.*, 2013, **36**, 75–79.
- T. Y. Yang, J. Liu, R. F. Zhou, Z. G. Chen, H. Y. Xu, S. Z. Qiao and M. J. Monteiro, *J. Mater. Chem. A*, 2014, **2**, 18139–18146.
- L. Zhang, J. Kim, E. Dy, S. Ban, K. C. Tsay, H. Kawai, Z. Shi and J. J. Zhang, *Electrochim. Acta*, 2013, **108**, 814–819.
- F. Pei, T. H. An, J. Zang, X. J. Zhao, X. L. Fang, M. S. Zheng, Q. F. Dong and N. F. Zheng, *Adv. Energy Mater.*, 2016, **6**, 1502539.
- J. Liang, X. Y. Yu, H. Zhou, H. B. Wu, S. J. Ding and X. W. Lou, *Angew. Chem., Int. Ed.*, 2014, **53**, 12803–12807.
- A. B. Fuertes, P. Valle-Vigón and M. Sevilla, *Chem. Commun.*, 2012, **48**, 6124–6126.
- H. W. Zhang, M. H. Yu, H. Song, O. Noonan, J. Zhang, Y. N. Yang, L. Zhou and C. Z. Yu, *Chem. Mater.*, 2015, **27**, 6297–6304.
- H. W. Zhang, O. Noonan, X. D. Huang, Y. N. Yang, C. Xu, L. Zhou and C. Z. Yu, *ACS Nano*, 2016, **10**, 4579–4586.
- H. H. Zhong, Y. Luo, S. He, P. G. Tang, D. Q. Li, N. Alonso-Vante and Y. J. Feng, *ACS Appl. Mater. Interfaces*, 2017, **9**, 2541–2549.
- C. J. Lei, Y. Wang, Y. Hou, P. Liu, J. Yang, T. Zhang, X. D. Zhuang, M. W. Chen, B. Yang, L. C. Lei, C. Yuan, M. Qiu and X. L. Feng, *Energy Environ. Sci.*, 2019, **12**, 149–156.
- X. X. Wang, D. A. Cullen, Y. T. Pan, S. Hwang, M. Y. Wang, Z. X. Feng, J. Y. Wang, M. H. Engelhard, H. G. Zhang, Y. Y. He, Y. Y. Shao, D. Su, K. L. More, J. S. Spendelov and G. Wu, *Adv. Mater.*, 2018, **30**, 1706758.